

## Construction of three-dimensional ternary reduced graphene oxide-g-C<sub>3</sub>N<sub>4</sub> nanosheets-AgBr aerogel for enhanced degradation of pollution under visible light

Zirong Luo, Zijun Zhong, Huijuan He, Dandan Li, Shaozao Tan, Langhuan Huang\*

Guangdong Engineering and Technology Research Centre of Graphene-like Materials and Products, Department of Chemistry, College of Chemistry and Materials Science, Jinan University, Guangzhou 510632, China, Tel. +86 13422068994; email: thuanglh@jnu.edu.cn (L.H. Huang), Tel. +86 13535554730; email: luozirong3@163.com (Z.R. Luo), Tel. +86 13411190188; email: zhongzi.jun@163.com (Z.J. Zhong), Tel. +86 18719130062; email: 1138373032@qq.com (H.J. He), Tel. +86 13631787221; email: WOW2863828@163.com (D.D. Li), Tel. +86 13925046829; email: tsztan@jnu.edu.cn (S.Z. Tan)

Received 30 March 2019; Accepted 26 July 2019

### ABSTRACT

In this study, a novel three-dimensional (3D) reduced graphene oxide-g-C<sub>3</sub>N<sub>4</sub> nanosheets-AgBr (RGO-CNN-AgBr) composite aerogel visible light photocatalyst was synthesized by hydrothermal method. In this ternary composite system, AgBr anchored onto g-C<sub>3</sub>N<sub>4</sub> nanosheets could improve the absorption rate of visible light and promote the separation of photogenerated electron-hole pairs simultaneously. The introduction of RGO could not only provide a fast channel for electron transfer, but also form a looser 3D porous structure, which could increase the specific surface area and cause the multiple reflections of incident light to promote absorption of light and adsorption of reactants. Based on these synergistic effects, the ternary composite photocatalyst exhibited excellent photodegradation properties. The results showed that under the same conditions, the removal rate of methyl orange by RGO-CNN-AgBr was improved to a certain extent relative to g-C<sub>3</sub>N<sub>4</sub> nanosheets (CNN), up to 90%. Furthermore, the photocatalytic activity of RGO-CNN-AgBr decreased only slightly after four degradations, revealing the excellent stability. The photocatalytic mechanism of RGO-CNN-AgBr was explained, which embodied the good prospect of this composite photocatalyst in the practical application of pollutant degradation.

**Keywords:** Reduced graphene oxide/g-C<sub>3</sub>N<sub>4</sub>/AgBr; Ternary photocatalyst; Visible-light photocatalyst; Graphitic carbon nitride

### 1. Introduction

In order to solve the growing environmental pollution problems, the development of a stable and efficient visible-light responsive photocatalyst has become one of the hotspots of photocatalysis research. [1–5]. In recent years, various semiconductors have been explored [6–12]. Graphitic carbon nitride (g-C<sub>3</sub>N<sub>4</sub>) has excellent chemical stability, thermal stability and suitable positions of valence band and conduction band [13–17]. However, the photocatalytic activity

of bulk g-C<sub>3</sub>N<sub>4</sub> was restricted by its low specific surface area, low solar absorption efficiency and the rapid recombination of photo-generated charge carriers. In order to improve the photocatalytic activity of g-C<sub>3</sub>N<sub>4</sub>, numerous strategies have been proposed. Some researches have shown that the two-dimensional structure of g-C<sub>3</sub>N<sub>4</sub> nanosheets (CNN) prepared from bulk g-C<sub>3</sub>N<sub>4</sub> can improve the photocatalytic performance to some extent [18–21]. Nevertheless, the photocatalytic activity of pure CNN still cannot satisfy the practical application. Coupling CNN with other semiconductor has been proved to be efficient to further improve the photocatalysis. It has been reported that AgBr with small

\* Corresponding author.

bandgap can expand the absorption range of visible light and is widely studied in photocatalysis [22–25]. In addition, three-dimensional (3D) graphene can provide better support for semiconductor photocatalysts. Moreover, with the capability of strong charge transfer, the graphene sheet can effectively separate the photo-generated charges, which greatly restrains the recombination of photo-generated pairs, thereby improving the photocatalytic efficiency. Based on the above advantages, the research on 3D graphene in the field of adsorption and photocatalysis has been widely concerned in recent years [26–31].

In this work, we constructed a 3D ternary porous reduced graphene oxide-g-C<sub>3</sub>N<sub>4</sub> nanosheets-AgBr (RGO-CNN-AgBr) aerogel photocatalyst with RGO, CNN and AgBr for the first time. Then under visible light irradiation ( $\lambda \geq 420$  nm), the photocatalytic activity of the prepared photocatalysts were evaluated by photocatalytic degradation of methyl orange (MO). The results showed that RGO-CNN-AgBr exhibited higher photocatalytic activity than pure CNN. Finally, based on the experiment, we theoretically explained the possible photocatalytic mechanism.

## 2. Experimental setup

### 2.1. Preparation of AgBr, CNN-AgBr, RGO-CNN and RGO-CNN-AgBr

Graphene oxide graphite (GO) was synthesized by an improved Hummers method [32]. CNN was prepared by thermal polycondensation of dicyandiamide according to the previously reported method and then treated by acid

treatment [33,34]. RGO-CNN-AgBr was synthesized by a two-step method. As shown in Fig. 1, 0.04 g GO was dissolved in 10 mL deionized water, and ultrasonic stirred for 30 min. The resulting GO solution was added into 10 mL of CNN suspension (15 mg mL<sup>-1</sup>) and stirred for 30 min. Then the homogeneous mixture was charged into a Teflon-lined autoclave and reacted at 180°C for 4 h to generate 3D aerogel RGO-CNN, which was marked as RGO-CNN. Secondly, the obtained RGO-CNN was immersed into 10 mL (2 mL ethanol and 8 mL deionized water) solution of 0.462 g CTAB at 60°C for 6 h. 0.32 g AgNO<sub>3</sub> was dissolved in 10 mL deionized water, then the CTAB/RGO-CNN was immersed into in AgNO<sub>3</sub> solution for 12 h. The prepared RGO-CNN-AgBr was washed several times by deionized water and then freeze-dried. Under the same conditions, CNN-AgBr without GO was prepared in the same manner and Preparation of pure AgBr by direct reaction with AgNO<sub>3</sub> and CTAB aqueous solution.

### 2.2. Characterizations

X-ray diffraction (XRD) patterns were obtained on X-ray diffractometer (RiRGOku Smartlab, 3 kW) with Cu-K $\alpha$  ( $\lambda = 1.5406$  Å) collected from 5° to 80°. A Nicolet 6700 spectrometer was used to record the Fourier-transform infrared (FTIR) spectra. The X-ray photoelectron spectra (XPS) was obtained with an ESCALAB-250 spectrometer. Brunauer–Emmett–Teller specific surface areas were measured by N<sub>2</sub> adsorption-desorption on an Autosorb iQ Station. The morphologies of samples were observed using field emission scanning electron microscopy (SEM) (JEOL JEM-7600F, Japan). The microstructures of the obtained samples were

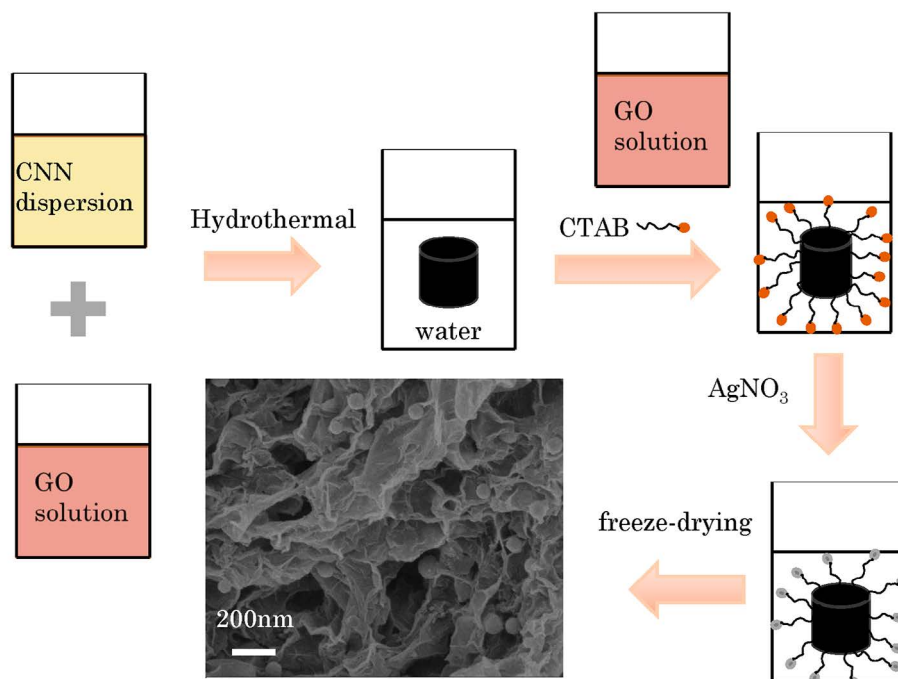


Fig. 1. Schematic diagram for synthesis of RGO-CNN-AgBr.

recorded using transmission electron microscopy (TEM, Philips Tecnai-10, Netherlands) and high-resolution TEM (JEOL 2010, Japan). A Hitachi 330 (Japan) UV-Vis spectrophotometer was used to perform the UV-Vis diffuse reflectance spectra (DRS, Japan). A Hitachi F-4500 (Japan) fluorescence spectrophotometer was used to measure the photoluminescence spectra (PL, Japan) at room temperature.

### 2.3. Photocatalytic degradation experiment

The photocatalytic performances of the samples were measured toward the degradation of the MO dye induced by a 300 W Xe lamp (Beijing, Tianmai Light Source Electrical Appliance Co.) with 420 nm cut-off filter. The temperature of the reaction solution was kept at 25°C. In a typical experiment, the RGO-CNN-AgBr was put into MO solution (30 mg L<sup>-1</sup>, 100 mL), then stirred in the dark for 1 h to reach the adsorption-desorption equilibrium. A small amount of supernatant was taken from each sample at regular intervals during the visible light irradiation. The solutions were measured at 465 nm using a UV-vis spectrophotometer. The  $C/C_0$  was used to describe the change in concentration, the rate of photocatalytic reaction could be expressed by Eq. (1):

$$\ln\left(\frac{C}{C_0}\right) = -kt \quad (1)$$

where  $C$  and  $C_0$  were the residual concentration and initial concentration of the dye after adsorption equilibrium, respectively;  $k$  (min<sup>-1</sup>) was the apparent reaction rate constant.

The photocatalytic stability was verified by four separate cycle runs. After photodegradation every 3 h, the photocatalyst was separated and washed with deionized water, lyophilized overnight to wait for the next run.

## 3. Results and discussion

### 3.1. XRD analysis

Fig. 2 showed the XRD patterns of AgBr, GO, CNN, RGO-CNN, CNN-AgBr and RGO-CNN-AgBr, respectively. For AgBr, the diffraction peaks appeared at 25.3°, 31.2°, 44.6°, 55.5°, 64.7° and 73.4° was correspond to the (111), (200), (220), (222), (400) and (311) planes of AgBr, respectively [35,36]. As for pure GO, a sharp diffraction peak corresponding to the (002) reflection was found near 10.13°. For CNN, the diffraction peak appeared at 27.4° could correspond to the (002) plane of graphite material and this was an obvious C-N network structure. Obviously, the main characteristic diffraction peaks originated from AgBr and CNN were both observed in RGO-CNN-AgBr. However, the (002) peak originated from CNN in RGO-CNN-AgBr displayed a markedly reduced intensity when compared with that in RGO-CNN and CNN-AgBr, which suggested that the introduction of RGO and AgBr changed the ordered structure of CNN and CNN had been successfully exfoliated. In addition, compared with pure AgBr, the (200) peak of AgBr in CNN-AgBr and RGO-CNN-AgBr got broadened, indicating that the particle size of AgBr decreased. This might be attributed to the abundant active sites from CNN and RGO and then

improved the desorption of AgBr. The above conclusions could be confirmed by the results of subsequent SEM and TEM. Moreover, no diffraction peaks from GO was found in RGO-CNN and RGO-CNN-AgBr. That's likely because GO was partially converted into RGO during the hydrothermal process and the diffraction peak of RGO was weak.

### 3.2. FTIR and XPS analysis

The chemical structure in the sample molecules were characterized by FTIR. As shown in Fig. 3, the bands of pure GO centered at 1,051–1,732 cm<sup>-1</sup> was related to the vibrational peaks of a large number of oxygen-containing functional groups [37]. For CNN, the bands within 1,200–1,600 cm<sup>-1</sup> were related to the stretching modes of CN heterocycles. Furthermore, the sharp peak at 809 cm<sup>-1</sup> and the broad band in the range of 3,000–3,500 cm<sup>-1</sup> were indicative of the triazine

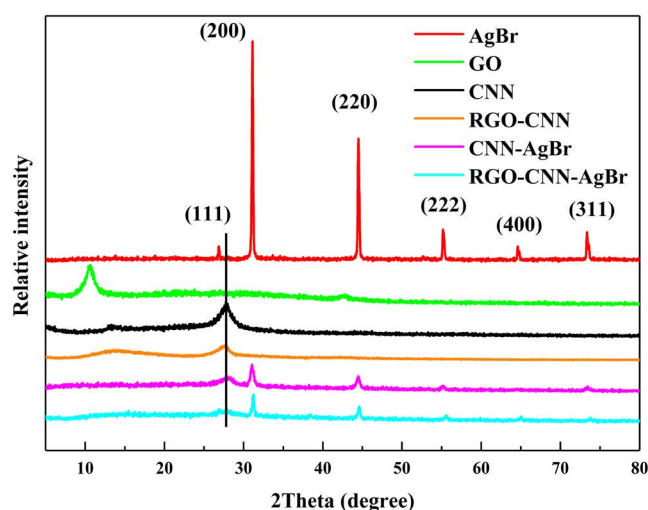


Fig. 2. XRD patterns of AgBr, GO, CNN, RGO-CNN, CNN-AgBr and RGO-CNN-AgBr.

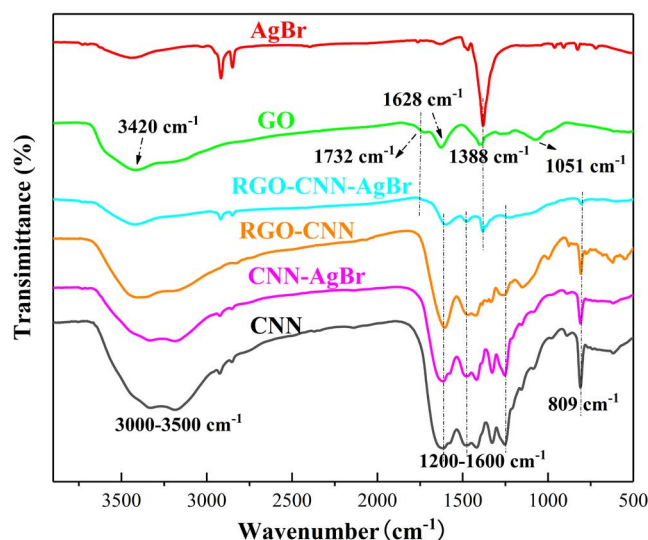


Fig. 3. FTIR spectra of AgBr, GO, CNN, RGO-CNN, CNN-AgBr and RGO-CNN-AgBr.

units and N–H stretch vibration modes, respectively [38,39]. The FTIR spectra of CNN-AgBr almost coincided with that of CNN, which indicated that these samples had the same chemical structure as CNN. For RGO-CNN and RGO-CNN-AgBr, the disappearance of some oxygen-containing functional groups was observed, meaning that they might be linked to RGO and CNN by conversion to covalent bonds during the reaction. At the same time, the above analysis and the characteristic peaks of AgBr and CNN appeared in the spectrum of RGO-CNN-AgBr, which comprehensively proved the successful synthesis of the ternary complex.

The XPS technique could further determine the chemical structure and elemental composition of RGO-CNN-AgBr.

Fig. 4a shows that RGO-CNN-AgBr contained the elements of C, O, N, Ag and Br, and their mass ratios were 44.43%, 12.41%, 20.35%, 17% and 5.8%, respectively. As shown in Fig. 4b, the  $sp^2$  C–C bond, C–OH and N–C=N bonds appeared at 284.8, 286.1 and 288.4 eV, respectively. Furthermore, in the C 1s spectrum, the peaks at 284.8 and 288.4 eV were mainly derived from  $g-C_3N_4$ , while the peak at 286.1 eV was originated in the residual C–OH bond from RGO after hydrothermal. The presence of C–OH bond was good agreement with the peak (531.9 eV) in O 1s spectrum from RGO-CNN-AgBr (Fig. 4c). Fig. 4d shows that the N 1s spectrum could be deconvoluted into three peaks, which demonstrated three types of N bonding in RGO-CNN-AgBr. Then the peaks at 398.7 and

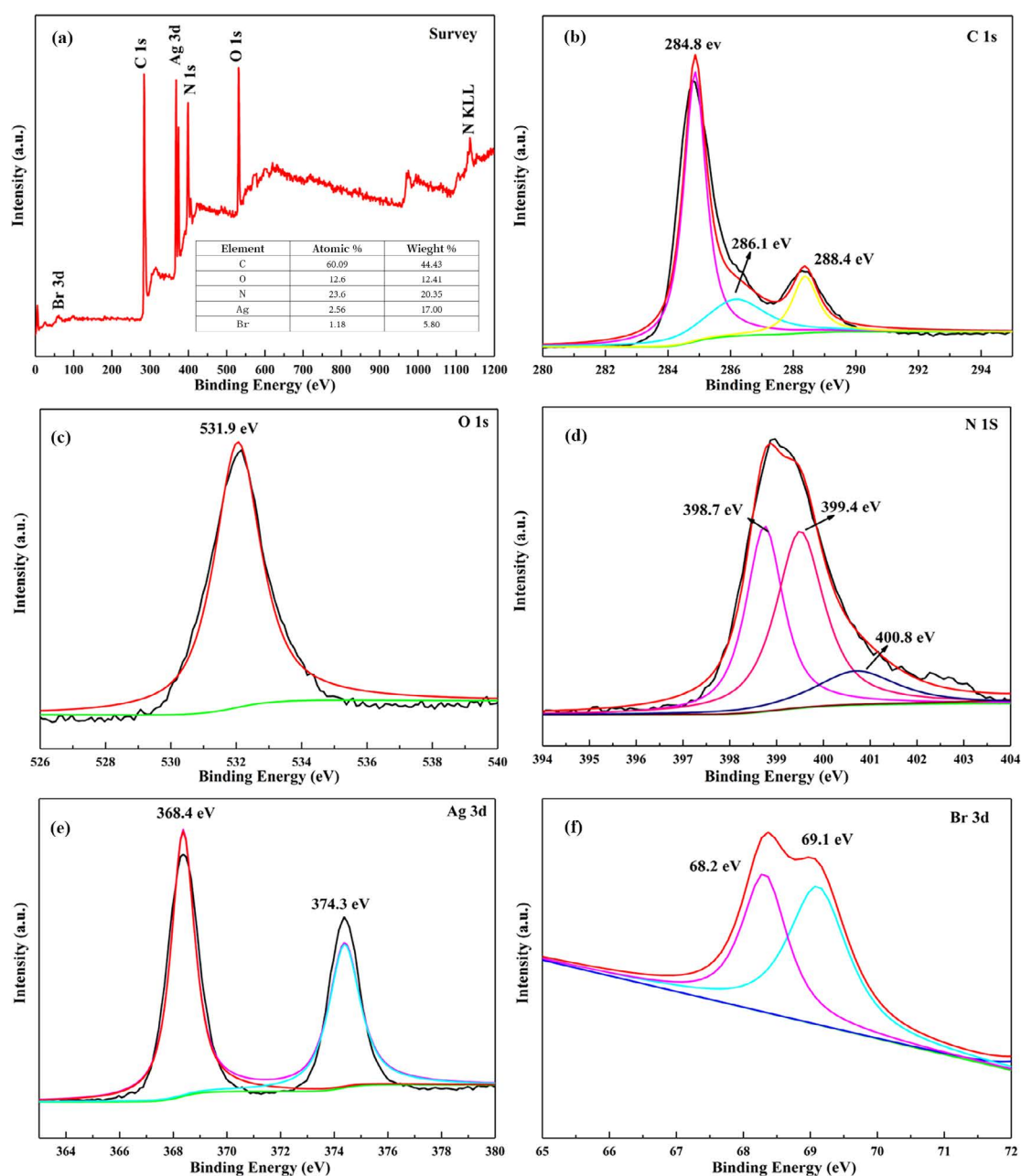


Fig. 4. XPS spectra of RGO-CNN-AgBr: survey, C 1s, O 1s, N 1s, Ag 3d and Br 3d, respectively (a–f).

399.4 eV were attributed to  $sp^2$ -hybridized in triazine rings (C–N=C) and tertiary nitrogen N ( $C_3$ ) groups, while amino groups (C–N–H) appeared at 400.8 eV. As shown in Fig. 4e, the Ag  $3d_{5/2}$  (binding energy 368.4 eV) and Ag  $3d_{3/2}$  (binding energy 374.3 eV) could be attributed to  $Ag^+$  of AgBr [40,28]. Furthermore, Br  $3d_{5/2}$  (binding energy 68.2 eV) and Br  $3d_{3/2}$  (binding energy 69.1 eV) in the Br 3d spectrum (Fig. 4f) are indicating good binding to AgBr [41].

### 3.3. Microtopography analysis

The observations of SEM and TEM could reveal the microstructures of the obtained samples. Fig. 5a shows that CNN

was composed of curved nanosheets. After the introduction of RGO, RGO-CNN exhibited an interconnected 3D network, which was looser than pure CNN (Fig. 5b). As shown in Figs. 5c and d, the RGO-CNN-AgBr had a fluffy and uniform porous microstructure and it had a black columnar macrostructure, which could support the weight of about 700 times its weight as depicted in the inset of Fig. 5c. Obviously, a large number of AgBr nanoparticles were uniformly distributed in the pores of the gel. The size of AgBr nanoparticles was uniform in the range of 100–150 nm. Fig. 5e shows the TEM images of RGO-CNN-AgBr, the AgBr nanoparticles were uniformly distributed on RGO-CNN, which was consistent with the SEM images. The spacing of the lattice fringes

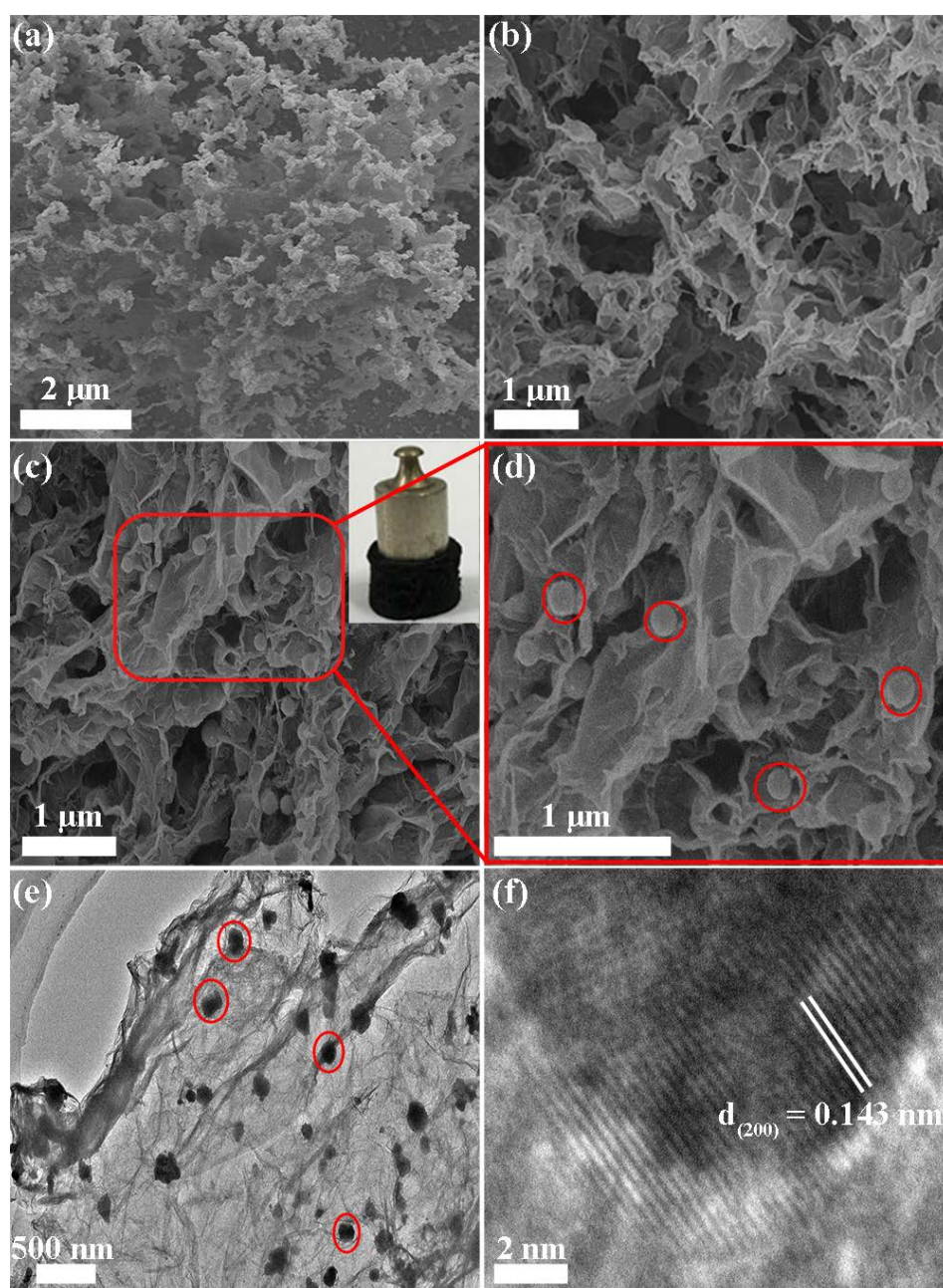


Fig. 5. SEM images of CNN, RGO-CNN and RGO-CNN-AgBr (a–d), TEM image (e) and HRTEM image (f) of RGO-CNN-AgBr.

(Fig. 5f) was about 0.143 nm, corresponding to the (200) plane of AgBr [42]. All the above results indicated that AgBr was successfully loaded into RGO-CNN gel.

The pore structure and specific surface area of RGO-CNN-AgBr were further analyzed by  $N_2$  adsorption-desorption isotherm experiments. As shown in Fig. 6, the isotherms of RGO-CNN-AgBr were type IV according to the Brunauer-Emmett-Deming-Teller (BDDT) classification, indicating RGO-CNN-AgBr possessed the porous property. Obviously, RGO-CNN-AgBr showed a high adsorption capacity in high relative pressure region, because of a slit formed by the stacking and winding of sheet CNN and RGO, which reflected the porous structure of aerogel. The inset in Fig. 6 shows that RGO-CNN-AgBr exhibited mesopores at about 4 nm thanks to the defect in CNN during acid treatment. RGO-CNN-AgBr had a large specific surface area ( $126.58 \text{ m}^2 \text{ g}^{-1}$ ) because of its abundant pore structure. The large specific surface area resulted in more reactive sites, which was beneficial

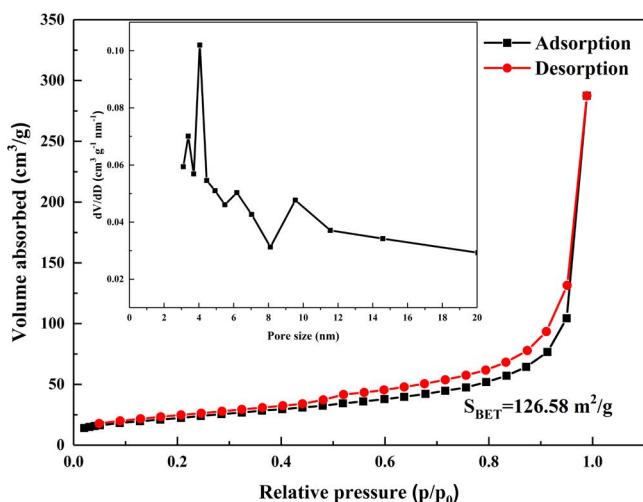
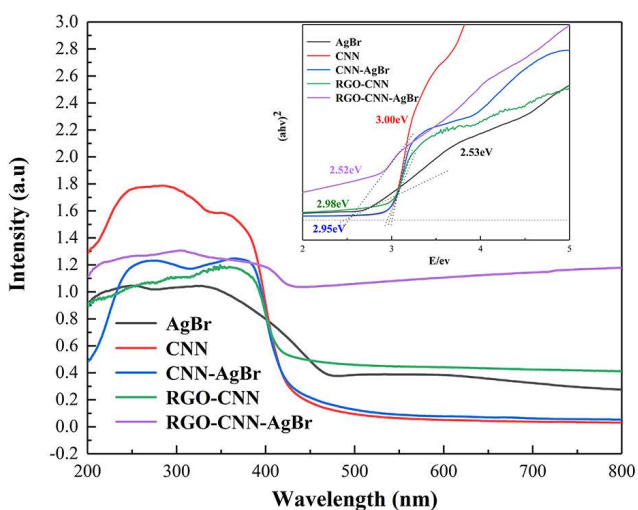


Fig. 6.  $N_2$  adsorption-desorption isotherm and BJH pore size distributions of RGO-CNN-AgBr.



to improve the photocatalytic activity and the absorption of pollutants.

### 3.4. Optical properties

UV-Vis absorption spectrum could test the optical properties of composites. As shown in Fig. 7a, CNN had a strong visible light absorption below 420 nm. Furthermore, the visible light absorption of CNN-AgBr and RGO-CNN increased when the AgBr and RGO were introduced separately. As shown in the inset of Fig. 7a, the band RGOp of AgBr, CNN, CNN-AgBr, RGO-CNN and RGO-CNN-AgBr were determined to be 2.53, 3.00, 2.95, 2.98 and 2.52 eV, respectively. Obviously, RGO-CNN-AgBr showed a red-shift of the absorption edge with respect to CNN, CNN-AgBr and RGO-CNN. And the introduction of RGO and AgBr led to an increase in the visible absorption. In addition, the interconnected pore structure in porous aerogel could reflect the incident light several times, which could further improve the visible light utilization.

The separation efficiency of photo-electrons and holes in the samples were studied by PL. Fig. 7b shows that a wide and strong peak of CNN appeared at 437 nm. Compared with CNN, the PL emission intensity of CNN-AgBr and RGO-CNN became much weaker, which indicated that introduction of AgBr or RGO could inhibit the photogenerated electron-hole recombination. The PL emission peak of RGO-CNN exhibited slightly blue shifted which might be the well-known quantum confinement effect. This indicated that in this ternary system, AgBr acted as an electron trapping trap, and RGO acted as a "highway" for generating electrons from CNN-AgBr, and the synergy between them greatly improved electron transport efficiency.

### 3.5. Photocatalytic activity and stability analysis

The photocatalytic activity of the synthesized photocatalysts was evaluated by the degradation of MO ( $30 \text{ mg L}^{-1}$ , 100 mL) under visible light. Fig. 8a shows that before the illumination, the dark adsorption was first performed for

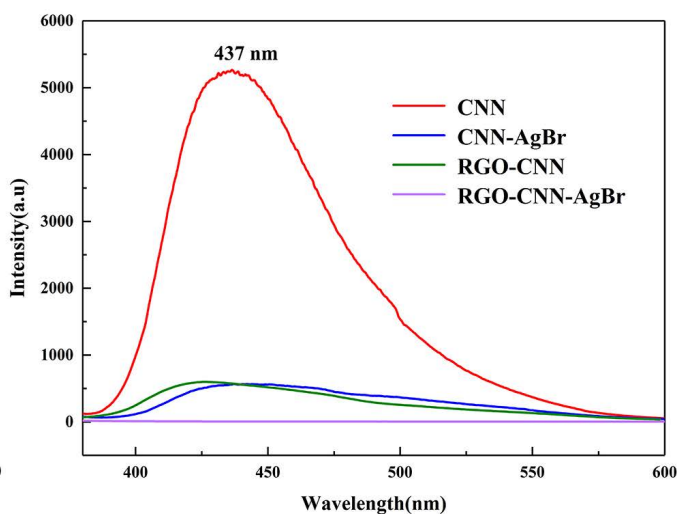


Fig. 7. UV-vis absorption spectrums (a) and PL emission spectrums (b) of CNN, CNN-AgBr, RGO-CNN and RGO-CNN-AgBr.

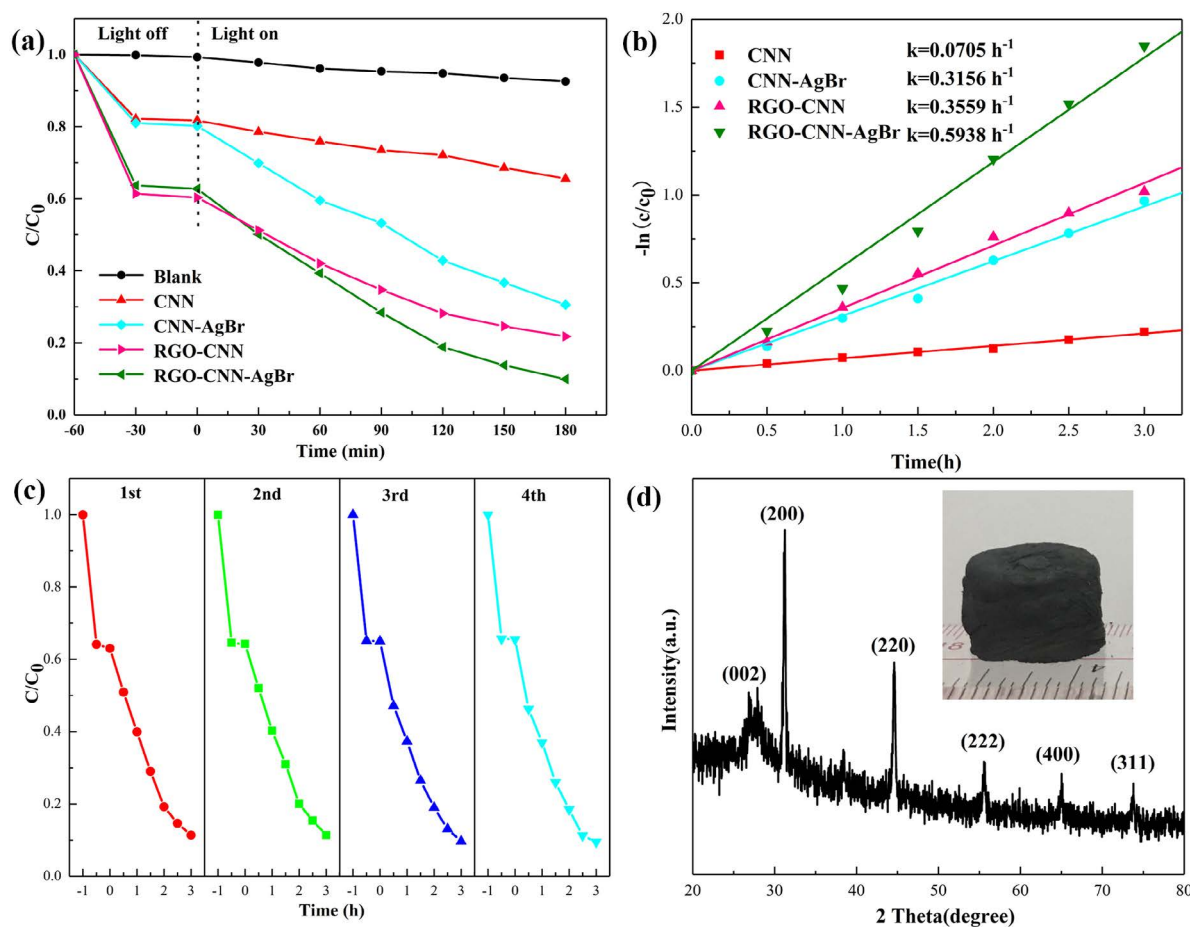


Fig. 8. Photocatalytic degradation of MO aqueous under visible light ( $\lambda \geq 420$  nm) over CNN, CNN-AgBr, RGO-CNN and RGO-CNN-AgBr (a), corresponding dynamics simulation curves (b) and cycles of the removal of MO by RGO-CNN-AgBr (c) The XRD pattern of the RGO-CNN-AgBr sample after 4th run cycle photocatalytic experiments (d), the digital image of the sample after 4th run cycle (the inset of d).

60 min to eliminate the interference of the adsorption on the photodegradation process, and the adsorption performance of the photocatalysts was observed. The adsorption equilibrium had been achieved in all photocatalysts within 60 min. As shown in Fig. 8a, RGO-CNN and RGO-CNN-AgBr displayed excellent absorptivity towards MO, which might be due to the introduction of RGO increased their specific surface area. After 3 h of illumination, the highest activity was obtained over RGO-CNN-AgBr, resulting 90% degradation for MO. Fig. 8b shows the photocatalytic reaction rate could be described by the pseudo-first-order kinetic equation. The reaction rate constant ( $k$ ) of RGO-CNN-AgBr was  $0.5938 \text{ h}^{-1}$ , which was about 8.4, 1.9 and 1.7 times higher than that of CNN, CNN-AgBr and RGO-CNN, respectively. In addition, the following experiments were carried out by running four different cycle experiments to test the photocatalyst stability, because of its importance in practical application. Fig. 8c shows that the photocatalytic activity of RGO-CNN-AgBr only exhibited a slight decrease after four cycles, indicating that the ternary composite photocatalyst had excellent application stability. In addition, the samples after four cycles were characterized by XRD analysis (Fig. 8d). As shown, there

was no significant difference in crystal structure and macro-structure of the samples after recycling (the inset of Fig. 8d).

### 3.6. Photocatalytic mechanism

In order to understand the active species produced during the degradation of RGO-CNN-AgBr, hydroxyl radicals ( $\cdot\text{OH}$ ), holes ( $h^+$ ) and superoxide radicals ( $\cdot\text{O}_2^-$ ) were captured with tert-butanol ( $t\text{-BuOH}$ ), triethanolamine (TEA) and 1,4-benzoquinones (BQ), respectively. The effects of different capture scavengers on the degradation of MO were shown in Fig. 9. After the addition of  $t\text{-BuOH}$ , the degradation rate of MO decreased slightly, indicating that there was almost no  $\cdot\text{OH}$  in the photocatalytic system. However, after the addition of TEA and BQ, the degradation rate decreased obviously, which indicated that  $\cdot\text{O}_2^-$  were the main active substances in the system, and together with  $h^+$  played an important role in the process of photodegradation.

AgBr and CNN are excited by visible light to generate photogenerated electrons  $e^-$  and holes  $h^+$ , respectively. As shown in Fig. 10, on the matching band structure, the photogenerated electrons originated from CNN were transferred

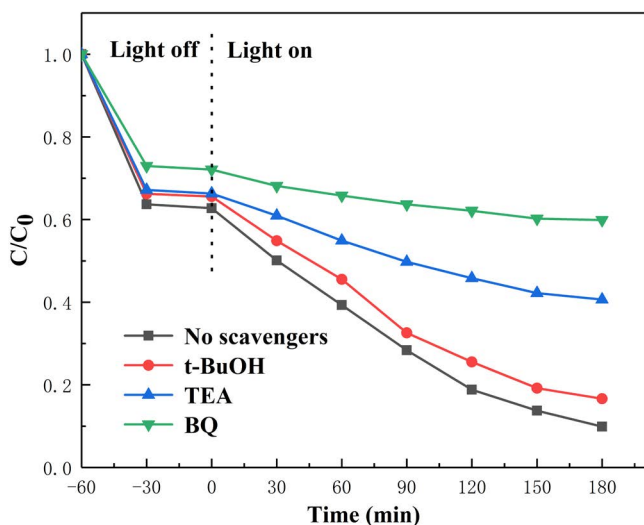


Fig. 9. Active species capture experiment of RGO-CNN-AgBr photocatalyst for degradation of MO under visible light irradiation.

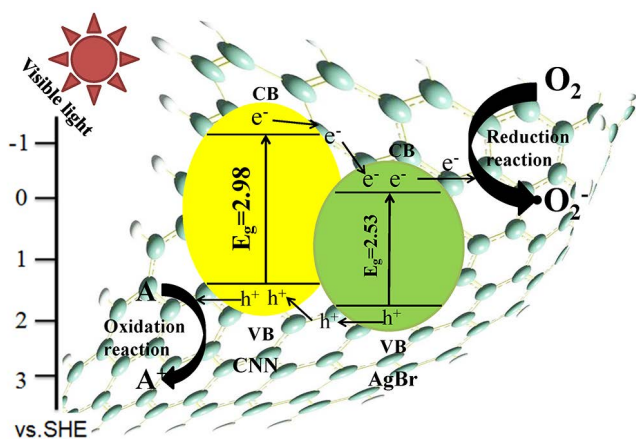


Fig. 10. Schematic diagram of RGO-CNN-AgBr about its photocatalytic activity mechanism.

to the conduction band of AgBr, and the  $\cdot\text{O}_2^-$  are produced. At the same time, the photogenerated holes originated from AgBr were transferred to the valence band of CNN. Finally, pollutants were oxidized by  $\cdot\text{O}_2^-$  and  $h^+$ . AgBr acted as an electron trapping promoted the separation of photogenerated electron-hole pairs. As for RGO, it provided a fast channel for electron transfer and further reduced the recombination rate of electron-hole pairs. Moreover, the combination of RGO resulted in a more loose and porous structure, increasing the specific surface area and causing multiple reflection of incident light. Based on these synergistic effects, the ternary composite photocatalyst exhibited excellent photodegradation properties for MO under visible light irradiation.

#### 4. Conclusion

A new 3D porous RGO-CNN-AgBr composite photocatalyst was prepared by hydrothermal method. The introduction

of RGO could not only rapidly transfer the photo-generated electrons, but also form a 3D porous structure, which could provide larger specific surface area and enhance the visible light absorption and the adsorption of reactant. Moreover, AgBr particles acted as electrons trap could promote the separation of photogenerated electron-hole pairs and enhance the absorption of visible light to some extent. The results of degradation of MO under visible light indicated that the degradation rate of MO by RGO-CNN-AgBr was about 9 times higher than CNN. More importantly, RGO-CNN-AgBr had a macroscopic block morphology, and the photocatalytic activity remained 90% after four cycles. It is believed that such a well-designed 3D porous RGO-CNN-AgBr composite photocatalyst has a good prospect in the practical application of pollutant degradation.

#### Acknowledgement

This study is supported by the Department of Science and Technology of Guangdong Province China [2016A010103047].

#### References

- [1] R. Jaiswal, N. Patel, A. Dashora, R. Fernandes, M. Yadav, R. Edla, R.S. Varma, D.C. Kothari, B.L. Ahuja, A. Miotello, Efficient Co-B-codoped  $\text{TiO}_2$  photocatalyst for degradation of organic water pollutant under visible light, *Appl. Catal., B*, 183 (2016) 242–253.
- [2] Y. Cao, Z.P. Xing, Y.C. Shen, Z.Z. Li, X.Y. Wu, X. Yan, J.L. Zou, S.L. Yang, W. Zhou, Mesoporous black  $\text{Ti}^{3+}/\text{N-TiO}_2$  spheres for efficient visible-light-driven photocatalytic performance, *Chem. Eng. J.*, 325 (2017) 199–207.
- [3] A. Akhundi, A. Habibi-Yangjeh, Novel  $g\text{-C}_3\text{N}_4/\text{Ag}_2\text{SO}_4$  nanocomposites: fast microwave-assisted preparation and enhanced photocatalytic performance towards degradation of organic pollutants under visible light, *J. Colloid Interface Sci.*, 482 (2016) 165–174.
- [4] S. Ahluwalia, N.T. Prakash, R. Prakash, B. Pal, Improved degradation of methyl orange dye using bio-co-catalyst Se nanoparticles impregnated ZnS photocatalyst under UV irradiation, *Chem. Eng. J.*, 306 (2016) 1041–1048.
- [5] M. Shekofteh-Gohari, A. Habibi-Yangjeh, M. Abitorabi, A. Rouhi, Magnetically separable nanocomposites based on ZnO and their applications in photocatalytic processes: a review, *Crit. Rev. Env. Sci. Technol.*, 48 (2018) 806–857.
- [6] Y. Liu, J.J. Kong, J.L. Yuan, W. Zhao, X. Zhu, C. Sun, J.M. Xie, Enhanced photocatalytic activity over flower-like sphere  $\text{Ag}/\text{Ag}_2\text{CO}_3/\text{BiVO}_4$  plasmonic heterojunction photocatalyst for tetracycline degradation, *Chem. Eng. J.*, 331 (2018) 242–254.
- [7] C.L. Wen, H.T. Zhang, Q.B. Bo, T.Z. Huang, Z.L. Lu, J.M. Lv, Y. Wang, Facile synthesis organic-inorganic heterojunctions of  $\text{HSbO}_3/g\text{-C}_3\text{N}_4$  as efficient visible-light-driven photocatalyst for organic degradation, *Chem. Eng. J.*, 270 (2015) 405–410.
- [8] S.Y. Dong, X.H. Ding, T. Guo, X.P. Yue, X. Han, J.H. Sun, Self-assembled hollow sphere shaped  $\text{Bi}_2\text{WO}_6/\text{RGO}$  composites for efficient sunlight-driven photocatalytic degradation of organic pollutants, *Chem. Eng. J.*, 316 (2017) 778–789.
- [9] M. Huang, J.H. Yu, Q. Hu, W.L. Su, M. Fan, B. Li, L.H. Dong, Preparation and enhanced photocatalytic activity of carbon nitride/titania(001 vs 101 facets)/reduced graphene oxide ( $g\text{-C}_3\text{N}_4/\text{TiO}_2/\text{rGO}$ ) hybrids under visible light, *Appl. Surf. Sci.*, 389 (2016) 1084–1093.
- [10] J.X. Low, J.G. Yu, M. Jaroniec, S. Wageh, A.A. Al-Ghamdi, Heterojunction photocatalysts, *Adv. Mater.*, 29 (2017) 1601694.
- [11] M. Pirhashemi, A. Habibi-Yangjeh, S.R. Pouran, Review on the criteria anticipated for the fabrication of highly efficient ZnO-based visible-light-driven photocatalysts, *J. Ind. Eng. Chem.*, 62 (2018) 1–25.

- [12] S. Asadzadeh-Khaneghah, A. Habibi-Yangjeh, D. Seifzadeh, Graphitic carbon nitride nanosheets coupled with carbon dots and BiOI nanoparticles: boosting visible-light-driven photocatalytic activity, *J. Taiwan Inst. Chem. Eng.*, 87 (2018) 98–111.
- [13] S.C. Yan, Z.S. Li, Z.G. Zou, Photodegradation performance of g-C<sub>3</sub>N<sub>4</sub> fabricated by directly heating melamine, *Langmuir*, 25 (2009) 10397–10401.
- [14] H.J. Yan, H.X. Yang, TiO<sub>2</sub>-g-C<sub>3</sub>N<sub>4</sub> composite materials for photocatalytic H<sub>2</sub> evolution under visible light irradiation, *J. Alloys Compd.*, 509 (2011) L26–L29.
- [15] W.-J. Ong, L.-L. Tan, Y.H. Ng, S.-T. Yong, S.-P. Chai, Graphitic carbon nitride (g-C<sub>3</sub>N<sub>4</sub>)-based photocatalysts for artificial photosynthesis and environmental remediation: are we a step closer to achieving sustainability?, *Chem. Rev.*, 116 (2016) 7159–7329.
- [16] L. Ge, C.C. Han, J. Liu, Y.F. Li, Enhanced visible light photocatalytic activity of novel polymeric g-C<sub>3</sub>N<sub>4</sub> loaded with Ag nanoparticles, *Appl. Catal., A*, 409 (2011) 215–222.
- [17] S. Asadzadeh-Khaneghah, A. Habibi-Yangjeh, M. Abedi, Decoration of carbon dots and AgCl over g-C<sub>3</sub>N<sub>4</sub> nanosheets: novel photocatalysts with substantially improved activity under visible light, *Sep. Purif. Technol.*, 199 (2018) 64–77.
- [18] F. Dong, Y.H. Li, Z.Y. Wang, W.-K. Ho, Enhanced visible light photocatalytic activity and oxidation ability of porous graphene-like g-C<sub>3</sub>N<sub>4</sub> nanosheets via thermal exfoliation, *Appl. Surf. Sci.*, 358 (2015) 393–403.
- [19] X.J. She, L. Liu, H.Y. Ji, Z. Mo, Y.P. Li, L.Y. Huang, D.L. Du, H. Xu, H.M. Li, Template-free synthesis of 2D porous ultrathin nonmetal-doped g-C<sub>3</sub>N<sub>4</sub> nanosheets with highly efficient photocatalytic H<sub>2</sub> evolution from water under visible light, *Appl. Catal., B*, 187 (2016) 144–153.
- [20] Y.C. Deng, L. Tang, C.Y. Feng, G.M. Zeng, J.J. Wang, Y.Y. Zhou, Y. Liu, B. Peng, H.P. Feng, Construction of plasmonic Ag modified phosphorous-doped ultrathin g-C<sub>3</sub>N<sub>4</sub> nanosheets/BiVO<sub>4</sub> photocatalyst with enhanced visible-near-infrared response ability for ciprofloxacin degradation, *J. Hazard. Mater.*, 344 (2018) 758–769.
- [21] Y.H. Li, W.K. Ho, K. Lv, B.C. Zhu, S.C. Lee, Carbon vacancy-induced enhancement of the visible light-driven photocatalytic oxidation of NO over g-C<sub>3</sub>N<sub>4</sub> nanosheets, *Appl. Surf. Sci.*, 430 (2018) 380–389.
- [22] F. Chen, Q. Yang, Y. Wang, J.W. Zhao, D.B. Wang, X.M. Li, Z. Guo, H. Wang, Y.C. Deng, C.G. Niu, G.M. Zeng, Novel ternary heterojunction photocatalyst of Ag nanoparticles and g-C<sub>3</sub>N<sub>4</sub> nanosheets co-modified BiVO<sub>4</sub> for wider spectrum visible-light photocatalytic degradation of refractory pollutant, *Appl. Catal., B*, 205 (2017) 133–147.
- [23] Y. Cao, Z.P. Xing, Z.Z. Li, X.Y. Wu, M.Q. Hu, X. Yan, Q. Zhu, S.L. Yang, W. Zhou, Mesoporous black TiO<sub>2</sub>-x/Ag nanospheres coupled with g-C<sub>3</sub>N<sub>4</sub> nanosheets as 3D/2D ternary heterojunctions visible light photocatalysts, *J. Hazard. Mater.*, 343 (2018) 181–190.
- [24] H. Xu, J. Yan, Y.G. Xu, Y.H. Song, H.M. Li, J.X. Xia, C.J. Huang, H.L. Wan, Novel visible-light-driven AgX/graphite-like C<sub>3</sub>N<sub>4</sub> (X = Br, I) hybrid materials with synergistic photocatalytic activity, *Appl. Catal., B*, 129 (2013) 182–193.
- [25] S.Y. Yang, W.Y. Zhou, C.Y. Ge, X.T. Liu, Y.P. Fang, Z.S. Li, Mesoporous polymeric semiconductor materials of graphitic-C<sub>3</sub>N<sub>4</sub>: general and efficient synthesis and their integration with synergistic AgBr NPs for enhanced photocatalytic performances, *RSC Adv.*, 3 (2013) 5631–5638.
- [26] W.J. Han, C. Zang, Z.Y. Huang, H. Zhang, L. Ren, X. Qi, J.X. Zhong, Enhanced photocatalytic activities of three-dimensional graphene-based aerogel embedding TiO<sub>2</sub> nanoparticles and loading MoS<sub>2</sub> nanosheets as Co-catalyst, *Int. J. Hydrogen Energy*, 39 (2014) 19502–19512.
- [27] B.C. Qiu, M.Y. Xing, J.L. Zhang, Mesoporous TiO<sub>2</sub> nanocrystals grown in situ on graphene aerogels for high photocatalysis and lithium-ion batteries, *J. Am. Chem. Soc.*, 136 (2014) 5852–5855.
- [28] Y. Fan, W. Ma, D. Han, S. Gan, X. Dong, L. Niu, Convenient recycling of 3D AgX/graphene aerogels (X = Br, Cl) for efficient photocatalytic degradation of water pollutants, *Adv. Mater.*, 27 (2015) 3767–3773.
- [29] Z.W. Tong, D. Yang, J.F. Shi, Y.H. Nan, Y.Y. Sun, Z.Y. Jiang, Three-dimensional porous aerogel constructed by g-C<sub>3</sub>N<sub>4</sub> and graphene oxide nanosheets with excellent visible-light photocatalytic performance, *ACS Appl. Mater. Interfaces*, 7 (2015) 25693–25701.
- [30] X. Yan, R.P. Xu, J.K. Guo, X. Cai, D.J. Chen, L.H. Huang, Y.Q. Xiong, S.Z. Tan, Enhanced photocatalytic activity of Cu<sub>2</sub>O/g-C<sub>3</sub>N<sub>4</sub> heterojunction coupled with reduced graphene oxide three-dimensional aerogel photocatalysis, *Mater. Res. Bull.*, 96 (2017) 18–27.
- [31] X. Li, J.G. Yu, S. Wageh, A.A. Al-Ghamdi, J. Xie, Graphene in photocatalysis: a review, *Small*, 12 (2016) 6640–6696.
- [32] W.S. Hummers Jr., R.E. Offeman, Preparation of graphitic oxide, *J. Am. Chem. Soc.*, 80 (1958) 1339–1339.
- [33] H. Zhang, L.X. Zhao, F.L. Geng, L.-H. Guo, B. Wan, Y. Yang, Carbon dots decorated graphitic carbon nitride as an efficient metal-free photocatalyst for phenol degradation, *Appl. Catal., B*, 180 (2016) 656–662.
- [34] F.X. Cheng, H. Wang, X.P. Dong, The amphoteric properties of g-C<sub>3</sub>N<sub>4</sub> nanosheets and fabrication of their relevant heterostructure photocatalysts by an electrostatic re-assembly route, *Chem. Commun.*, 51 (2015) 7176–7179.
- [35] Y.X. Yang, W. Guo, Y. Guo, Y.H. Zhao, X. Yuan, Y.H. Guo, Fabrication of Z-scheme plasmonic photocatalyst Ag@AgBr/g-C<sub>3</sub>N<sub>4</sub> with enhanced visible-light photocatalytic activity, *J. Hazard. Mater.*, 271 (2014) 150–159.
- [36] H.X. Shi, J.Y. Chen, G.Y. Li, X. Nie, H.J. Zhao, P.-K. Wong, T.C. An, Synthesis and characterization of novel plasmonic Ag/AgX-CNIs (X = Cl, Br, I) nanocomposite photocatalysts and synergetic degradation of organic pollutant under visible light, *ACS Appl. Mater. Interfaces*, 5 (2013) 6959–6967.
- [37] H.-L. Guo, X.-F. Wang, Q.-Y. Qian, F.-B. Wang, X.-H. Xia, A green approach to the synthesis of graphene nanosheets, *ACS Nano*, 3 (2009) 2653–2659.
- [38] J. Fu, B. Chang, Y. Tian, F. Xi, X. Dong, Novel C<sub>3</sub>N<sub>4</sub>-CdS composite photocatalysts with organic-inorganic heterojunctions: in situ synthesis, exceptional activity, high stability and photocatalytic mechanism, *J. Mater. Chem. A*, 1 (2013) 3083–3090.
- [39] G.Z. Liao, S. Chen, X. Quan, H.T. Yu, H.M. Zhao, Graphene oxide modified g-C<sub>3</sub>N<sub>4</sub> hybrid with enhanced photocatalytic capability under visible light irradiation, *J. Mater. Chem.*, 22 (2012) 2721–2726.
- [40] X.L. Xiao, L. Ge, C.C. Han, Y.J. Li, Z. Zhao, Y.J. Xin, S. Fang, L. Wu, P. Qiu, A facile way to synthesize Ag@AgBr cubic cages with efficient visible-light-induced photocatalytic activity, *Appl. Catal., B*, 163 (2015) 564–572.
- [41] H.Y. Li, S.Y. Gan, H.Y. Wang, D.X. Han, L. Niu, Intercorrelated superhybrid of AgBr supported on graphitic-C<sub>3</sub>N<sub>4</sub>-decorated nitrogen-doped graphene: high engineering photocatalytic activities for water purification and CO<sub>2</sub> reduction, *Adv. Mater.*, 27 (2015) 6906–6913.
- [42] D.M. Chen, Z.H. Wang, Y. Du, G.L. Yang, T.Z. Ren, H. Ding, In situ ionic-liquid-assisted synthesis of plasmonic photocatalyst Ag/AgBr/g-C<sub>3</sub>N<sub>4</sub> with enhanced visible-light photocatalytic activity, *Catal. Today*, 258 (2015) 41–48.